
Integrating GNN and Neural ODEs for Estimating Two-Body Interactions in Mixed-Species Collective Motion

Masahito Uwamichi
 Graduate School of Arts and Sciences
 The University of Tokyo
 uwamichi@g.ecc.u-tokyo.ac.jp

Simon K. Schnyder
 Institute of Industrial Science
 The University of Tokyo
 simon@sat.t.u-tokyo.ac.jp

Tetsuya J. Kobayashi
 Institute of Industrial Science
 The University of Tokyo
 tetsuya@sat.t.u-tokyo.ac.jp

Satoshi Sawai
 Graduate School of Arts and Sciences
 The University of Tokyo
 cssawai@mail.ecc.u-tokyo.ac.jp

Abstract

Analyzing the motion of multiple biological agents, be it cells or individual animals, is pivotal for the understanding of complex collective behaviors. With the advent of advanced microscopy, detailed images of complex tissue formations involving multiple cell types have become more accessible in recent years. However, deciphering the underlying rules that govern cell movements is far from trivial. Here, we present a novel deep learning framework to estimate the underlying equations of motion from observed trajectories, a pivotal step in decoding such complex dynamics. Our framework integrates graph neural networks with neural differential equations, enabling effective prediction of two-body interactions based on the states of the interacting entities. We demonstrate the efficacy of our approach through two numerical experiments. First, we used a simulated data from a toy model to tune the hyperparameters. Based on the obtained hyperparameters, we then applied this approach to a more complex model that describes interacting cells of cellular slime molds. Our results show that the proposed method can accurately estimate the function of two-body interactions, thereby precisely replicating both individual and collective behaviors within these systems.

1 Introduction

Collective motion, a phenomenon observed in various biological systems, is characterized by the coordinated movement of multiple entities. This behavior is prevalent in a wide range of systems[26], from flocks of birds[5, 11, 7] and schools of fish[15] to cellular slime molds[12], microswimmers[10], and human crowds[17]. Understanding the underlying mechanisms of collective motion is crucial for elucidating the principles governing the dynamics of these systems. In particular, the interactions between individual entities play a pivotal role in shaping the collective behavior of the system.

Recent advances in imaging technologies have enabled detailed observations at the cellular level, providing insights into the dynamics of complex tissue formation involving multiple cell types. For example, cellular slime molds, a model organism for studying collective motion, exhibit intricate behaviors such as aggregation, migration, and differentiation[12]. These behaviors are driven by the interactions between different cell types, which are mediated by chemical signals and physical

forces. Decoding the underlying equations of motion governing these interactions is essential for understanding the emergent properties of these systems.

In this work, we present a novel deep learning framework for estimating two-body interactions in mixed-species collective motion. Our framework integrates graph neural networks (GNNs) with neural differential equations (neural DEs) to predict the interactions between pairs of entities based on their states. GNNs are well-suited for modeling complex interactions in graph-structured data, while neural DEs provide a flexible framework for learning the dynamics of the system. By combining these two approaches, we can effectively capture the interactions between individual entities and predict their collective behavior. We demonstrate the efficacy of our framework through two numerical experiments. The first experiment uses a toy model designed to generate data for refining the hyperparameters of our framework. The second experiment explores a complex scenario mimicking the collective motion of cellular slime molds, where two different cell types interact with each other. Our results show that our method can accurately estimate the two-body interactions, thereby replicating both individual and collective behaviors within these systems.

The rest of this paper is organized as follows. In Section 2, we introduce the study of collective motion. In section 3, we provide an overview of related work on collective motion and deep learning for dynamical systems. In Section 4, we describe our deep learning framework for estimating two-body interactions in mixed-species collective motion. In Section 5, we present the results of our numerical experiments. Finally, in Section 6, we discuss the implications of our work and outline future research directions.

2 Background

Let us first describe the formulation of collective motion in active matter. Starting with the Vicsek model [25], the collective behavior in active matter is described based on the centroids, velocities, and orientations of each individual. A unique aspect of active matter is that it allows for the spontaneous generation of forces and torques, which is justified by the ability to extract and utilize energy from the external environment[21]. The Vicsek model itself is a multi-particle model in discrete time, where each individual possesses a velocity along its orientation and adjusts its direction based on interactions with nearby individuals. This model assumes that interactions among individuals are local and can be represented using a graph structure[1]. Stemming from this model, numerous other models have been proposed, differing in the nature of interactions between individuals and the forms of their equations of motion. Particularly models with continuous-time motion equations often use Langevin equations where the motion of individuals is described by the summation of pairwise interactions[8]. Furthermore, since active matter can utilize energy from the external environment, focusing solely on the moving agents categorizes it as an open system. This implies that the conservation of total system energy is not required, making these systems inherently unsuitable for Hamiltonian descriptions. Given this background, the formulation of collective motion in active matter typically involves direct descriptions of forces rather than using free energy.

3 Related Work

This section discusses methods for estimating governing laws from data, commonly referred to as system identification. System identification aims to estimate the equations of motion of a system from data. One well-known method for estimating differential equations is Sparse Identification of Nonlinear Dynamics (SINDy) [6]. SINDy estimates nonlinear differential equations from data using LASSO regression to sparsely estimate the terms of the equations. However, when applying this method to many-body systems with pairwise interactions, the number of parameters to estimate increases exponentially with the number of individuals, which raises computational costs and leads to potential instabilities. Other system identification methods use Bayesian optimization [3, 4, 2], e.g. representing the functions in the motion equations through basis function expansion, and estimating their coefficients via Bayesian optimization. This method has been successfully used in Vicsek model, reproducing its formation of orientational order. However, the effectiveness of this approach for more complex systems, such as mixed-species systems, remains unclear. Deep learning approaches to analyzing collective motion have also been proposed [13, 24, 18]. These incorporate Attention mechanisms to analyze behaviors limited to turning right or left [13], systems that limit the scope to Vicsek-type models to estimate orientational order parameters [24], or to

estimate two-body interaction as a function of and those using Hamiltonians to estimate repulsive forces [18]. Nevertheless, these methods have limitations regarding the types of systems they can be applied to or the specific behaviors they can estimate. Particularly, no methods have been proposed so far that can be applied to systems where multiple species interact in unknown ways.

4 Method

The goal of this study is to estimate the rules of motion for individual entities within collective motion data. We represent the state of each entity i at time t as $\mathcal{Z} \ni z^i(t) = (x^i(t), y^i) \in \mathcal{X} \times \mathcal{Y}$, where $x^i \in \mathcal{X}$ denotes the variables described by the motion equations in the state space $\mathcal{X} \subset \mathbb{R}^n$, and y^i , a non-temporal variable, represents auxiliary attributes such as the type of each entity within the feature space \mathcal{Y} . We define a distance function $d : \mathcal{Z} \times \mathcal{Z} \rightarrow \mathbb{R}$, and assume that entities i and j interact if $d(z^i(t), z^j(t)) < d_0$, where $d_0 \in \mathbb{R}$ is a predefined threshold. Consequently, the system at any time t can be represented as an undirected graph $G(t) = (V, E(t), Z(t))$, where $V = \{1, 2, \dots, N\}$ is the set of entities, $E(t) \subset V \times V$ denotes the pairs of interacting entities, and $Z(t) = \{z^i(t) | i \in V\}$ is the set of states of all entities. The motion of each entity $i \in V$ is governed by the following Langevin equation:

$$dx^i = \left(F^{(1)}(z^i(t)) + \sum_{j \text{ s.t. } (i,j) \in E(t)} F^{(2)}(z^i(t), z^j(t)) \right) dt + \sigma dW^i(t), \quad (1)$$

where $F^{(1)} : \mathcal{Z} \rightarrow \mathbb{R}^n$ represents self-driven forces, $F^{(2)} : \mathcal{Z} \times \mathcal{Z} \rightarrow \mathbb{R}^n$ encapsulates the forces due to interactions between pairs, $\sigma \in \mathbb{R}$ is the intensity of noise, and $W^i(t) \in \mathbb{R}^n$ is a Wiener process.

Given the initial state $Z(t_0) \in \mathcal{Z}$ at time $t_0 \in \mathbb{R}$, the state $Z(t_0 + \Delta t) \in \mathcal{Z}$ after a time interval $\Delta t \in \mathbb{R}$ can be determined by solving the motion equation using the operator $S(F^{(1)}, F^{(2)}, \sigma, d, d_0) : (Z(t_0), \Delta t) \mapsto Z(t_0 + \Delta t)$. Here, $z^i(t_0 + \Delta t) = (x^i(t_0 + \Delta t), y^i)$ is defined by the following integral:

$$x^i(t_0 + \Delta t) = x^i(t_0) + \int_{t_0}^{t_0 + \Delta t} dx^i(t), \quad (2)$$

which is computed numerically. For $\sigma = 0$, we use the neural ordinary differential equation (neural ODE) method[9, 23], and for $\sigma \neq 0$ the neural stochastic differential equation (neural SDE) method[19, 16]. The summation over $E(t)$ in the equations is efficiently calculated using a graph neural network (GNN) based on the message passing algorithm. To facilitate these computations within the neural DE frameworks, we developed a wrapper using a GNN framework, deep graph library[27]. This wrapper computes the set $E(t)$ using the provided $z(t)$, d , and d_0 , and then calculates and returns the summation of forces $F^{(1)}$ and $F^{(2)}$. In particular, this constitutes a concrete implementation of $S(F^{(1)}, F^{(2)}, \sigma, d, d_0)$.

4.1 Simulation with a Given Model

Initially, we used the developed wrapper to conduct simulations with a predefined model. Specific forms for the interaction and distance functions $F_{\text{sim}}^{(1)}$, $F_{\text{sim}}^{(2)}$, and d_{sim} were provided, and appropriate settings for the noise magnitude σ_{sim} and threshold $d_{0,\text{sim}}$ were configured to construct $S_{\text{sim}} = S(F_{\text{sim}}^{(1)}, F_{\text{sim}}^{(2)}, \sigma_{\text{sim}}, d_{\text{sim}}, d_{0,\text{sim}})$. For each $i \in V$, initial states $x^i(0) \in \mathcal{X}_0$ were assigned uniformly at random, and appropriate values for $y^i \in \mathcal{Y}$ were also specified. Using S_{sim} , the motion equations were solved. The simulation was repeated M times, and the m -th result was denoted as $Z_{\text{sim}}^m : t \mapsto S_{\text{sim}}(Z_{\text{sim}}^m(0), t)$ with the m -th initial condition $Z_{\text{sim}}^m(0)$. The combined data set $Z_{\text{sim}} = \{Z_{\text{sim}}^m | m = 1, \dots, M\}$ was then used to apply the subsequent learning algorithm, aiming to estimate $F_{\text{sim}}^{(1)}$ and $F_{\text{sim}}^{(2)}$.

4.2 Learning Algorithm

Subsequently, we developed a learning algorithm to estimate $F_{\text{sim}}^{(1)}$ and $F_{\text{sim}}^{(2)}$ using the results from the simulations conducted. The self-propulsion and interaction functions, $F_{\text{NN}}^{(1)}$ and $F_{\text{NN}}^{(2)}$, were modeled

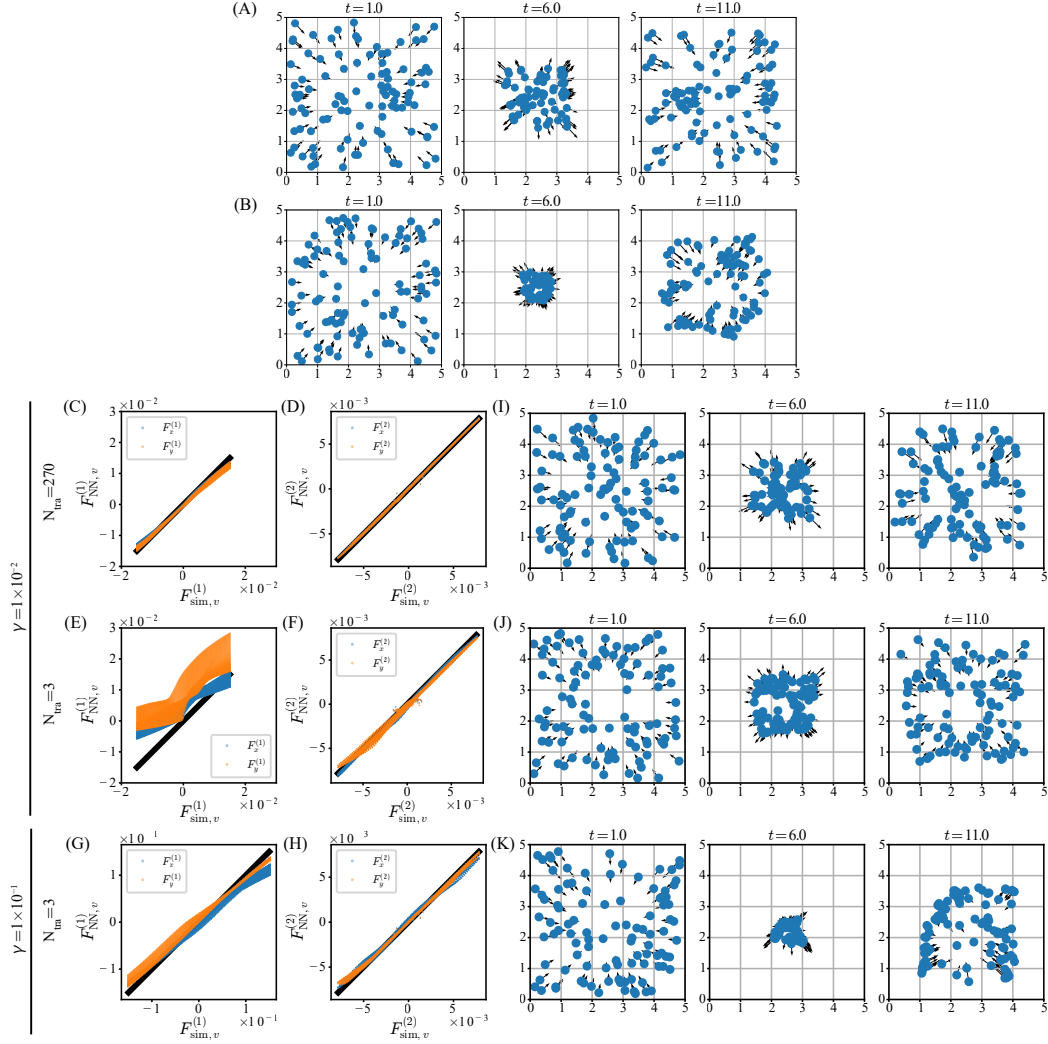


Figure 1: Snapshots of the simulation results in the harmonic interaction model with friction constants. (A) The case with a friction constant of $\gamma = 1 \times 10^{-2}$ and (B) with $\gamma = 1 \times 10^{-1}$. Positions of individuals are indicated by blue circles, and velocities by black arrows. (C-H) The functions estimated from the data with harmonic interaction plotted against the true values. The upper panel displays $F^{(1)}$ and the lower panel $F^{(2)}$ for different cases: (C-D) with $\gamma = 1 \times 10^{-2}$ and $N_{\text{tra}} = 270$, (E-F) with $\gamma = 1 \times 10^{-2}$ and $N_{\text{tra}} = 3$, and (G-H) with $\gamma = 1 \times 10^{-1}$ and $N_{\text{tra}} = 3$. Blue and orange indicates x- or y- element F . A black line serves as a guide indicating where the estimated values equal the true values. (I-K) Snapshots of the simulation results in the model estimated from the data with harmonic interaction. The panels represent different scenarios: (I) with $\gamma = 1 \times 10^{-2}$ and $N_{\text{tra}} = 270$, (J) with $\gamma = 1 \times 10^{-2}$ and $N_{\text{tra}} = 3$, and (K) with $\gamma = 1 \times 10^{-1}$ and $N_{\text{tra}} = 3$.

using neural networks. Unless otherwise specified, these functions consisted of a three-layer fully connected network followed by a scaling layer. Each fully connected layer consisted of 128 nodes, with the Exponential Linear Unit (ELU) serving as the activation function. The scaling layer involved a scalar A and a vector B as parameters, and it transformed an input vector $\alpha \in \mathbb{R}^n$ to $e^A \alpha + B$. This configuration allowed the output of the fully connected network to be scaled appropriately, reflecting physical scales.

The parameters of the fully connected networks and the scaling layer, collectively denoted as θ , were optimized to approximate $F_{\text{NN}}^{(1)}(\theta)$ and $F_{\text{NN}}^{(2)}(\theta)$ to $F_{\text{sim}}^{(1)}$ and $F_{\text{sim}}^{(2)}$, respectively. To evaluate the deviation of $F_{\text{NN}}^{(1)}(\theta)$ and $F_{\text{NN}}^{(2)}(\theta)$, we first solved the motion equations using these functions.

Specifically, we constructed $S_{\text{NN}}(\theta) = S(F_{\text{NN}}^{(1)}(\theta), F_{\text{NN}}^{(2)}(\theta), 0, d_{\text{sim}}, d_{0,\text{NN}})$ and used it to perform simulations. Here, $d_{0,\text{NN}}$ was a suitably set threshold, and for simplicity, $\sigma_{\text{NN}} = 0$. In the simulation, the initial state was set as $Z_{\text{sim}}^m(t_0)$, and we used this to compute the state τ time units later as $Z_{\text{NN}}^m(\theta; t_0 + \tau) = S_{\text{NN}}(\theta)(Z_{\text{sim}}^m(t_0), \tau)$.

A loss function $\mathcal{L} : \mathcal{Z} \times \mathcal{Z} \rightarrow \mathbb{R}$ was used to evaluate the discrepancy between the solution by θ and the simulation data through $\mathcal{L}^m(\theta; t_0) = \mathcal{L}(Z_{\text{sim}}^m(t_0 + \tau), Z_{\text{NN}}^m(\theta; t_0 + \tau))$. To optimize θ , the average $\mathcal{L}(\theta)$ of this loss function over various m and t_0 was minimized:

$$\theta^* = \arg \min_{\theta} \mathcal{L}(\theta) \quad (3)$$

The M simulation data sets were split into two parts, with M_{tra} sets used as training data and M_{val} sets used as validation data. This optimization was conducted using the LAMB optimization algorithm[28], leveraging gradient information with respect to θ . The parameter θ^* was evaluated using the minimum of the loss function calculated on the validation data set.

5 Experiments

In this section, we describe two numerical experiments to demonstrate the efficacy of the proposed method.

5.1 Underdamped Brownian Motion with Harmonic Interaction

First, to demonstrate that the self-propulsion and interaction forces could be estimated using our method, we performed simulations using a toy model. We used $N = 100$ particles, each with position $r^i(t) \in \mathbb{R}^2$ and velocity $v^i(t) \in \mathbb{R}^2$, such that $z^i(t) = x^i(t) = (r^i(t), v^i(t))$ and y^i is empty. The particles were connected by harmonic oscillators, and each velocity was subjected to a damping force, so the equations of motion read:

$$dr^i = v^i dt, \quad (4)$$

$$dv^i = \left(-\gamma v^i - \sum_{j \text{ s.t. } (i,j) \in E(t)} \nabla_{r^i} U(r^i - r^j) \right) dt + \sigma dW^i(t), \quad (5)$$

$$U(r) = \frac{1}{2} k (|r| - r_c)^2 \quad (6)$$

where $k \in \mathbb{R}$ is the strength of the interaction, $r_c \in \mathbb{R}$ the natural spring length, and $\gamma \in \mathbb{R}$ the friction coefficient. The distance function was $d_{\text{sim}}(z^i, z^j) = |r^i - r^j|$, with a threshold set at $d_{0,\text{sim}} = 5$.

In order to fit these terms into the aforementioned framework, the equations were reformulated as:

$$F_{\text{sim}}^{(1)}(z^i) = (F_{\text{sim},r}^{(1)}(z^i), F_{\text{sim},v}^{(1)}(z^i)) = (v^i, -\gamma v^i), \quad (7)$$

$$F_{\text{sim}}^{(2)}(z^i, z^j) = (F_{\text{sim},r}^{(2)}(z^i, z^j), F_{\text{sim},v}^{(2)}(z^i, z^j)) = (0, -\nabla_{r^i} U(r^i - r^j)). \quad (8)$$

Here, $k = 1 \times 10^{-3}$, $r_c = 1$, $\sigma = 1 \times 10^{-3}$, and γ was set to 1×10^{-2} or 1×10^{-1} . The initial states $x^i(0)$ were uniformly sampled from $\mathcal{X}_0 = [0, 5]^2 \times [0, 1 \times 10^{-3}]$, and simulations were performed to obtain Z_{sim} .

For these simulations, the Euler-Maruyama method with a time step of 0.1 was used, and data were collected at $t = 0, 1, \dots, 50$. The data showed that all particles cyclically gathered towards the center before dispersing (Figure 1(A-B)). When $\gamma = 1 \times 10^{-2}$, the amplitude of aggregation-dispersion was nearly constant (Figure 1(A), Supplemental Movie S1), whereas for $\gamma = 1 \times 10^{-1}$, the amplitude of aggregation-dispersion decreased (Figure 1(B), Supplemental Movie S2).

With these data, we applied our proposed method to estimate $F_{\text{sim}}^{(1)}$ and $F_{\text{sim}}^{(2)}$. $F_{\text{NN}}^{(1)}$ and $F_{\text{NN}}^{(2)}$ were modeled as follows:

$$F_{\text{NN}}^{(1)}(z^i; \theta) = (v^i, F_{\text{NN},v}^{(1)}(v^i; \theta)), \quad (9)$$

$$F_{\text{NN}}^{(2)}(z^i, z^j; \theta) = (0, F_{\text{NN},v}^{(2)}(r^j - r^i; \theta)). \quad (10)$$

$F_{\text{NN},v}^{(1)}$ and $F_{\text{NN},v}^{(2)}$ were each independent neural networks. We evaluated the predictive accuracy for position and velocity as follows, using $Z_{\text{NN}}^m(\theta; t_0 + \tau)$ predicted for $\tau = 10$ and the simulation data $Z_{\text{sim}}^m(t_0)$:

$$\mathcal{L}_r(Z_{\text{sim}}^m(t_0 + \tau), Z_{\text{NN}}^m(\theta; t_0 + \tau)) = \frac{1}{N} \sum_{i \in V} |r_{\text{NN}}^i(\theta; t_0 + \tau) - r_{\text{sim}}^i(t_0 + \tau)|^2, \quad (11)$$

$$\mathcal{L}_v(Z_{\text{sim}}^m(t_0 + \tau), Z_{\text{NN}}^m(\theta; t_0 + \tau)) = \frac{1}{N} \sum_{i \in V} |v_{\text{NN}}^i(\theta; t_0 + \tau) - v_{\text{sim}}^i(t_0 + \tau)|^2. \quad (12)$$

We sampled these metrics for 60 randomly selected pairs (m, t_0) . The total loss function $\mathcal{L}(\theta)$ for one batch was defined as the dimensionless sum of these metrics, normalized by the variance in the simulation data:

$$\mathcal{L}_r(\theta) = \sum_{(m, t_0)} \mathcal{L}_r(Z_{\text{sim}}^m(t_0 + \tau), Z_{\text{NN}}^m(\theta; t_0 + \tau)) / \text{Var}_{i, (m, t_0)}[r_{\text{sim}}^i(t_0 + \tau)], \quad (13)$$

$$\mathcal{L}_v(\theta) = \sum_{(m, t_0)} \mathcal{L}_v(Z_{\text{sim}}^m(t_0 + \tau), Z_{\text{NN}}^m(\theta; t_0 + \tau)) / \text{Var}_{i, (m, t_0)}[v_{\text{sim}}^i(t_0 + \tau)], \quad (14)$$

$$\mathcal{L}(\theta) = \mathcal{L}_r(\theta) + \mathcal{L}_v(\theta). \quad (15)$$

To minimize the loss function, we manually searched for optimal hyperparameters for the LAMB optimizer. We determined that $\beta_1 = 0.5$, $\beta_2 = 0.4$, $\epsilon = 1 \times 10^{-6}$, and a learning rate of 1×10^{-3} effectively minimized the loss function, although convergence was notably slow. It is important to note that we were unable to identify hyperparameters that would allow for both faster convergence and adequate estimation of the functional forms of $F^{(1)}$ and $F^{(2)}$. As a result of minimizing this loss function, we optimized θ to estimate $F_{\text{NN}}^{(1)}$ and $F_{\text{NN}}^{(2)}$ (Figure 1 (C-H)). When $\gamma = 1 \times 10^{-2}$ and the training set size was $M_{\text{tra}} = 270$ and validation set size $M_{\text{val}} = 30$, after 300 epochs (15 days), $F_{\text{NN},v}^{(1)}$ and $F_{\text{NN},v}^{(2)}$ were observed to approximate $F_{\text{sim},v}^{(1)}$ and $F_{\text{sim},v}^{(2)}$ respectively (Figure 1(C-D)). In contrast, with $M_{\text{tra}} = 3$ and $M_{\text{val}} = 3$, especially $F_{\text{NN},v}^{(1)}$ did not approximate $F_{\text{sim},v}^{(1)}$ even after 6000 epochs (4 days; Figure 1(E-F)). However, under the same dataset size but with $\gamma = 1 \times 10^{-1}$, $F_{\text{NN},v}^{(1)}$ and $F_{\text{NN},v}^{(2)}$ were confirmed to approximate $F_{\text{sim},v}^{(1)}$ and $F_{\text{sim},v}^{(2)}$ (Figure 1(G-H)).

The accuracy of the estimation results is quantified in Supplemental Table S1. For each particle or pair in the dataset Z_{sim} , we calculated the forces $F_v^{(1)}$ and $F_v^{(2)}$ and computed the Mean Squared Error (MSE) and Mean Absolute Error (MAE). These errors were then normalized by the L1 or L2 norm of $F_{\text{sim},v}^{(1)}$ and $F_{\text{sim},v}^{(2)}$ respectively, to provide dimensionless measures of accuracy. Due to the extensive computation time required for estimation, comprehensive statistics could not be gathered. Instead, we present the results of all trials to illustrate the trends in estimation accuracy. As observed, when $M_{\text{tra}} = 3$ with a low friction constant $\gamma = 1 \times 10^{-2}$, significant estimation errors occurred. Conversely, the estimation errors for the interaction force $F_v^{(2)}$ were largely unaffected by γ , suggesting that the estimation of interaction and friction are somewhat independent. However, when $M_{\text{tra}} = 270$, a slight improvement in the accuracy of interaction estimates was noted compared to the $M_{\text{tra}} = 3$ scenario. This observation indicates that not only friction but also the accuracy of interaction estimates depend on the number of data points used.

Furthermore, to verify how well these estimates fit the simulation data, we sampled random initial values $Z(0)$ in a similar manner to training data creation, conducted simulations, and visualized the results $S_{\text{NN}}(\theta^*)(Z(0), t)$ (Figure 1(I-K); Supplemental Movies S3-5). In all cases, the estimates were confirmed to adequately replicate the simulation data for all cases, even with $\gamma = 1 \times 10^{-2}$ and $M_{\text{tra}} = 3$. The ability to replicate simulation data suggests that friction had almost no effect in this case. However, this implies that the proposed method may not adequately estimate very weak effects.

5.2 Mixed Species Collective Motion with Overdamped Self-propulsion

Next, to test the proposed method in complex systems involving interactions among multiple species, we conducted simulations using a more complex model that emulates real collective movements. In this model, each of the $N = 400$ individuals has position $r^i(t) \in [0, L]^2$, orientation $\phi^i(t) \in$

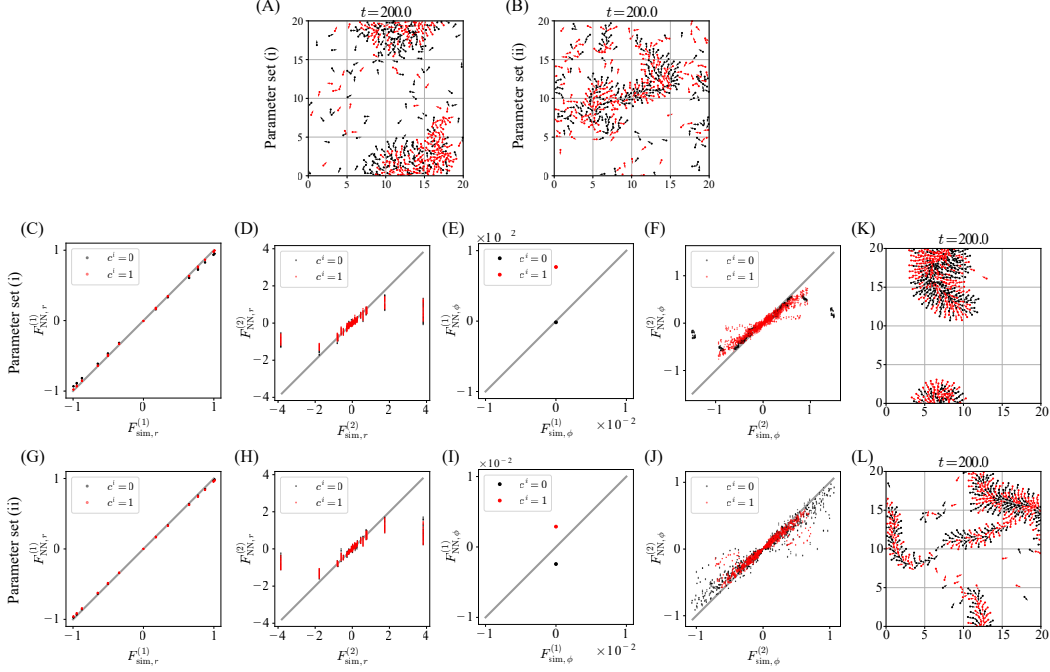


Figure 2: Snapshots of the simulation results in the mixed-species model. Panel (A) displays the case with parameter set (i), and panel (B) with parameter set (ii). Each individual is represented by an arrow located at their position and directed toward their polarity. Black arrows indicate individuals with $c^i = 0$, while red arrows represent those with $c^i = 1$. (C-J) The functions estimated from the data with the mixed-species model plotted against the true values. The rows display different cases: (C-F) with parameter set (i), and (G-J) with parameter set (ii). A gray line serves as a guide indicating where the estimated values equal the true values. (K-L) Snapshots of the simulation results in the model estimated from data with the mixed-species model. (K) The case with parameter set (i), and (L) with parameter set (ii).

$[0, 2\pi]$, and species type $c^i \in \{0, 1\}$. Both r^i and ϕ^i are subject to periodic boundary conditions, ensuring continuous and consistent movement dynamics across the defined space. This defines $x^i(t) = (r^i(t), \phi^i(t))$ and $y^i = (c^i)$, constituting $z^i(t) = (x^i(t), y^i)$. The motion equations for individual i are described as follows:

$$dr^i = (v_0 p^i + \sum_{js.t.(i,j) \in E(t)} \beta J_{\text{eV}}^{ij}) dt, \quad (16)$$

$$d\phi^i = - \sum_{js.t.(i,j) \in E(t)} \left(\alpha_{\text{CF}}(c^i) J_{\text{CF}}^{ij} + \alpha_{\text{Ch}}(c^i) J_{\text{Ch}}^{ij} \right) (r^{ij} \cdot p_{\perp}^i) dt + \sigma dW^i(t), \quad (17)$$

$$J_{\text{eV}}^{ij} = (r_c^{-1} - |r^{ij}|^{-1}) r^{ij}, \quad (18)$$

$$J_{\text{CF}}^{ij} = \frac{1}{2} \left(1 - \frac{r^{ij} \cdot p^j}{|r^{ij}|} \right), \quad (19)$$

$$J_{\text{Ch}}^{ij} = - \frac{r^{ij} \cdot p^i}{|r^{ij}|} K_1(\kappa |r^{ij}|), \quad (20)$$

$$p^i = (\cos \phi^i, \sin \phi^i), p_{\perp}^i = (-\sin \phi^i, \cos \phi^i), \quad (21)$$

$$r^{ij} = r^j - r^i \in [-L/2, L/2]^2. \quad (22)$$

with self-propulsion speed $v_0 \geq 0$, the strength of the excluded volume interaction $\beta \geq 0$, the strengths of contact following and chemotaxis $\alpha_{\text{CF}}, \alpha_{\text{Ch}} \geq 0$, respectively, the diffusion length of the chemoattractant $\kappa \geq 0$, the noise strength $\sigma \geq 0$, and the modified Bessel function of the second kind K_1 . The model was obtained by introducing a chemotaxis term into a preexisting model [14], to make it more appropriate for cellular slime molds. The chemotaxis term assumes rapid diffusion

of chemotactic substances secreted by each individual [20]. We varied the sensitivity of contact following and chemotaxis depending on the species type, thus modeling a system where different species interact. The interaction terms were adapted into our framework as follows:

$$F_{\text{sim}}^{(1)}(z^i) = (F_{\text{sim},r}^{(1)}(z^i), F_{\text{sim},\phi}^{(1)}(z^i)) \quad (23)$$

$$= (v_0 p^i, 0), \quad (24)$$

$$F_{\text{sim}}^{(2)}(z^i, z^j) = (F_{\text{sim},r}^{(2)}(z^i, z^j), F_{\text{sim},\phi}^{(2)}(z^i, z^j)) \quad (25)$$

$$= (\beta J_{\text{eV}}^{ij}, -(\alpha_{\text{CF}}(c^i) J_{\text{CF}}^{ij} - \alpha_{\text{Ch}}(c^i) J_{\text{Ch}}^{ij})(r^{ij} \cdot p_{\perp}^i)). \quad (26)$$

The distance function was $d_{\text{sim}}(z^i, z^j) = |r^{ij}|$, with periodic boundary conditions of width $L = 20$ and a threshold $d_{0,\text{sim}} = 1$. The parameters were $v_0 = 1$, $\beta = 1$, $\kappa = 0.5$, and $\sigma = \sqrt{0.2}$, with 200 individuals of each species $c^i = 0, 1$. Parameter dependencies based on c^i are shown in Supplemental Table S2.

The initial states $x^i(0)$ were uniformly sampled from $[0, L]^2 \times [0, 2\pi]$, and simulations were carried out to generate Z_{sim} using the Heun method with a timestep of 0.1, collecting data for $t = 0, 1, \dots, 300$. Simulation results for parameter set (i) showed the formation of mixed-species circular clusters exhibiting rotational behavior (Figure 2(A), Supplemental Movie S6). Conversely, results for parameter set (ii) formed centipede-like clusters of mixed species that moved translationally in local alignments (Figure 2(B), Supplemental Movie S7).

Using this data, we applied our method to estimate $F_{\text{sim}}^{(1)}$ and $F_{\text{sim}}^{(2)}$, modeling $F_{\text{NN}}^{(1)}$ and $F_{\text{NN}}^{(2)}$ as follows:

$$F_{\text{NN}}^{(1)}(z^i; \theta) = (\mathcal{R}(\phi^i) F_{\text{NN},r}^{(1)}(c^i; \theta), F_{\text{NN},\phi}^{(1)}(c^i; \theta)), \quad (27)$$

$$F_{\text{NN}}^{(2)}(z^i, z^j; \theta) = \begin{pmatrix} \mathcal{R}(\phi^i) F_{\text{NN},r}^{(2)}(\mathcal{R}(-\phi^i) r^{ij}, \phi^j - \phi^i, c^i, c^j; \theta) \\ F_{\text{NN},\phi}^{(2)}(\mathcal{R}(-\phi^i) r^{ij}, \phi^j - \phi^i, c^i, c^j; \theta) \end{pmatrix}^T. \quad (28)$$

Here, $F_{\text{NN},r}^{(1)}$, $F_{\text{NN},\phi}^{(1)}$, $F_{\text{NN},r}^{(2)}$, $F_{\text{NN},\phi}^{(2)}$ are independent neural networks with their respective parameters, and $\mathcal{R}(\phi^i)$ is the rotation matrix for ϕ^i , which converts all angles into relative angles with respect to ϕ^i , thereby maintaining the model's invariance to coordinate rotation. Additionally, when inputting the categorical variable c^i into the neural network, it is transformed into a two-dimensional vector via an embedding layer. The predictions $Z_{\text{NN}}^m(\theta; t_0 + \tau)$ made by this neural network for $\tau = 1$ and the simulation data $Z_{\text{sim}}^m(t_0)$ defined the prediction errors for position and orientation as follows:

$$\mathcal{L}_r(Z_{\text{sim}}^m(t_0 + \tau), Z_{\text{NN}}^m(\theta; t_0 + \tau)) = \frac{1}{N} \sum_{i \in V} d(r_{\text{NN}}^i(\theta; t_0 + \tau), r_{\text{sim}}^i(t_0 + \tau))^2, \quad (29)$$

$$\mathcal{L}_\phi(Z_{\text{sim}}^m(t_0 + \tau), Z_{\text{NN}}^m(\theta; t_0 + \tau)) = \frac{1}{N} \sum_{i \in V} (1 - \cos(\phi_{\text{NN}}^i(\theta; t_0 + \tau) - \phi_{\text{sim}}^i(t_0 + \tau))). \quad (30)$$

Predictions were computed using the Euler-Maruyama method with a timestep of 0.1. These metrics were sampled for 60 randomly selected pairs (m, t_0) and each was normalized by the variance in the simulation data to compose the loss function for one batch:

$$\mathcal{L}_r(\theta) = \sum_{(m, t_0)} \mathcal{L}_r(Z_{\text{sim}}^m(t_0 + \tau), Z_{\text{NN}}^m(\theta; t_0)) / \text{Var}_{i, (m, t_0)}[r_{\text{sim}}^i(t_0 + \tau)], \quad (31)$$

$$\mathcal{L}_\phi(\theta) = \sum_{(m, t_0)} \mathcal{L}_\phi(Z_{\text{sim}}^m(t_0 + \tau), Z_{\text{NN}}^m(\theta; t_0)) / \sum_{i, (m, t_0)} (1 - \cos(\phi_{\text{sim}}^i(t_0 + \tau))), \quad (32)$$

$$\mathcal{L}(\theta) = \mathcal{L}_r(\theta) + \mathcal{L}_\phi(\theta). \quad (33)$$

To minimizing this loss function, we tried the same hyperparameters as those used for the harmonic interaction model, and found we optimized θ to estimate $F_{\text{NN}}^{(1)}$ and $F_{\text{NN}}^{(2)}$ (Figure 2(C-J)). All experiments were conducted with $M_{\text{tra}} = 3$, $M_{\text{val}} = 3$. After 20,000 epochs (25 days), $F_{\text{NN},r}^{(1)}$, $F_{\text{NN},\phi}^{(1)}$, $F_{\text{NN},r}^{(2)}$, $F_{\text{NN},\phi}^{(2)}$ were found to approximate $F_{\text{sim},r}^{(1)}$, $F_{\text{sim},\phi}^{(1)}$, $F_{\text{sim},r}^{(2)}$, $F_{\text{sim},\phi}^{(2)}$ closely (Figure 2(C-J)). To further verify the fit of our estimation results with the simulation data, we sampled random initial values $Z(0)$ similarly to the training data creation process and conducted simulations to visualize the outcomes

$S_{\text{NN}}(\theta^*)(Z(0), t)$ (Figure 2(K-L); Supplemental Movies S8-9). The results confirmed that all estimates adequately reproduced the simulation data.

To further test the predictive power of the model trained on the mixed state, we performed simulations where all individuals were of the same type. For initial conditions $Z_c(0)$ where all $N = 400$ individuals shared the same type $c^i = c$, either $c = 0$ or $c = 1$, we performed simulations $S_{\text{sim}}(Z_c(0), t)$ and $S_{\text{NN}}(\theta^*)(Z_c(0), t)$, visualizing each case (Supplemental Figure S1). For parameter set (i) with $c^i = 0$, both $S_{\text{sim}}(Z_0(0), t)$ and $S_{\text{NN}}(\theta^*)(Z_0(0), t)$ showed the formation of two clusters that exhibited rotational movements (Supplemental Figure S1(A-B)). Conversely, for parameter set (i) with $c^i = 1$ and parameter set (ii) with $c^i = 0, 1$, both $S_{\text{sim}}(Z_0(0), t)$ and $S_{\text{NN}}(\theta^*)(Z_0(0), t)$ formed centipede-like clusters that moved translationally in alignment with their local direction (Supplemental Figure S1(C-H)). Finally, as a negative control, we conducted simulations where both types of individuals shared the same parameters, as in parameter sets (iii)-(v), and performed estimations using the neural network for each case (Supplemental Figure S2). In all instances, it was confirmed that $F_{\text{NN},r}^{(1)}, F_{\text{NN},\phi}^{(1)}, F_{\text{NN},r}^{(2)}, F_{\text{NN},\phi}^{(2)}$ closely approximated $F_{\text{sim},r}^{(1)}, F_{\text{sim},\phi}^{(1)}, F_{\text{sim},r}^{(2)}, F_{\text{sim},\phi}^{(2)}$. Notably, these estimation results showed minimal dependency on c^i in $F_{\text{NN}}^{(1)}(z^i; \theta^*), F_{\text{NN}}^{(2)}(z^i, z^j; \theta^*)$. This outcome suggests that the species dependency of interactions estimated by the proposed method in mixed assemblies is based on actual data, rather than being an artifact of the methodology.

As detailed in Supplemental Table S3, we quantified the estimation accuracy for each trial, similar to the methods described in Section 5.1. To note, since $F_{\text{sim},\phi}^{(1)} = 0$, the MSE and MAE for $F_{\phi}^{(1)}$ are not normalized. Our results demonstrate that $F_r^{(1)}$ is estimated with high accuracy across all conditions. Also, the estimation of $F_{\phi}^{(1)}$ is maintained at sufficiently small magnitudes relative to the order of magnitude (10^0) typically seen with $F_{\phi}^{(2)}$ (Figure 2(F,J)). Regarding the interactions, both $F_r^{(2)}$ and $F_{\phi}^{(2)}$ exhibited somewhat higher errors, approximately of the order of 10^{-1} . These errors likely stem from the high dimensionality of the inputs to the $F_{\text{NN}}^{(2)}$, which may prevent the neural network from achieving sufficient learning, or from the training process neglecting the noise.

6 Conclusion

In this study, we proposed a novel method for estimating interactions among individuals within models of collective motion. This method combines dynamic graph neural networks with Neural Ordinary Differential Equations (Neural ODEs) to estimate interactions among individuals. We demonstrated that this method could estimate interactions in both simple models and complex mixed-species collective motion models. In models with simple harmonic interactions, the proposed method was able to identify crucial interactions effectively. Particularly, in the complex mixed-species collective motion model, it was estimated that individuals of different species exhibited distinct interactions, demonstrating the efficacy of the proposed method. One limitation of this approach is the extensive time required for estimation. Moreover, the method currently estimates deterministic motion equations and only considers pairwise interactions, thereby not accommodating interactions among three or more bodies or the effects of noise. Future research is expected to extend this approach to estimate more general interactions and develop methods for stochastic motion equations.

Acknowledgements

This research was supported by JSPS KAKENHI Grant Numbers JP22H05673 awarded to MU, JP22H04841 and JP22K14012 awarded to SKS, JP19H05799 awarded to TJK, and JP19H05801 and JP19KK0282 awarded to SS. Additionally, support was provided by JST CREST Grant Numbers JPMJCR2011 to TJK and JPMJCR1923 to SS. We acknowledge the use of ChatGPT and GitHub Copilot for their assistance in swiftly articulating ideas and refining them into clear, comprehensible English text. The content was subsequently reviewed and finalized by the authors.

References

- [1] S Boccaletti, V Latora, Y Moreno, M Chavez, and D Hwang. Complex networks: Structure and dynamics. *Physics Reports*, 424(4-5):175–308, February 2006.

- [2] David B. Brückner, Nicolas Arlt, Alexandra Fink, Pierre Ronceray, Joachim O. Rädler, and Chase P. Broedersz. Learning the dynamics of cell–cell interactions in confined cell migration. *Proceedings of the National Academy of Sciences of the United States of America*, 118(7):e2016602118, February 2021.
- [3] David B. Brückner, Alexandra Fink, Christoph Schreiber, Peter J. F. Röttgermann, Joachim O. Rädler, and Chase P. Broedersz. Stochastic nonlinear dynamics of confined cell migration in two-state systems. *Nature Physics*, 15(6):595–601, June 2019.
- [4] David B. Brückner, Pierre Ronceray, and Chase P. Broedersz. Inferring the dynamics of underdamped stochastic systems. *Physical Review Letters*, 125(5):058103, July 2020.
- [5] Andrea Cavagna, Alessio Cimarelli, Irene Giardina, Giorgio Parisi, Raffaele Santagati, Fabio Stefanini, and Massimiliano Viale. Scale-free correlations in starling flocks. *Proceedings of the National Academy of Sciences of the United States of America*, 107:11865–11870, June 2010.
- [6] Kathleen Champion, Bethany Lusch, J. Nathan Kutz, and Steven L. Brunton. Data-driven discovery of coordinates and governing equations. *Proceedings of the National Academy of Sciences of the United States of America*, 116(45):22445–22451, November 2019.
- [7] Henry J. Charlesworth and Matthew S. Turner. Intrinsically motivated collective motion. *Proceedings of the National Academy of Sciences*, 116:15362–15367, 2019.
- [8] Hugues Chaté, Francesco Ginelli, Guillaume Grégoire, and Franck Raynaud. Collective motion of self-propelled particles interacting without cohesion. *Physical Review E*, 77(4):046113, 2008.
- [9] Ricky TQ Chen, Yulia Rubanova, Jesse Bettencourt, and David K Duvenaud. Neural ordinary differential equations. *Advances in neural information processing systems*, 31, 2018.
- [10] J. Elgeti, R. G. Winkler, and G. Gompper. Physics of microswimmers - single particle motion and collective behavior: A review. *Reports on Progress in Physics*, 78, May 2015.
- [11] Andrea Flack, Máté Nagy, Wolfgang Fiedler, Iain D Couzin, and Martin Wikelski. From local collective behavior to global migratory patterns in white storks. *Science*, 360(6391):911–914, 2018.
- [12] Taihei Fujimori, Akihiko Nakajima, Nao Shimada, and Satoshi Sawai. Tissue self-organization based on collective cell migration by contact activation of locomotion and chemotaxis. *Proceedings of the National Academy of Sciences of the United States of America*, 116(10):4291–4296, March 2019.
- [13] Francisco J. H. Heras, Francisco Romero-Ferrero, Robert C. Hinz, and Gonzalo G. de Polavieja. Deep attention networks reveal the rules of collective motion in zebrafish. *PLoS Computational Biology*, 15(9):e1007354, September 2019.
- [14] Tetsuya Hiraiwa. Dynamic self-organization of idealized migrating cells by contact communication. *Physical Review Letters*, 125(26):268104, 2020.
- [15] Yael Katz, Kolbjørn Tunstrøm, Christos C Ioannou, Cristián Huepe, Iain D Couzin, Simon A Levin, I D C Designed, and I D C Performed. Inferring the structure and dynamics of interactions in schooling fish. *Proceedings of the National Academy of Sciences*, 108:18720–18725, 2011.
- [16] Patrick Kidger, James Foster, Xuechen Li, Harald Oberhauser, and Terry Lyons. Neural sdes as infinite-dimensional gans. *International Conference on Machine Learning*, 2021.
- [17] Ven Jyn Kok, Mei Kuan Lim, and Chee Seng Chan. Crowd behavior analysis: A review where physics meets biology. *Neurocomputing*, 177:342–362, 2016.
- [18] Hiroshi Koyama, Hisashi Okumura, Atsushi M. Ito, Kazuyuki Nakamura, Tetsuhisa Otani, Kagayaki Kato, and Toshihiko Fujimori. Effective mechanical potential of cell–cell interaction explains three-dimensional morphologies during early embryogenesis. *PLoS Computational Biology*, 19(8):e1011306, August 2023.
- [19] Xuechen Li, Ting-Kam Leonard Wong, Ricky T. Q. Chen, and David Duvenaud. Scalable gradients for stochastic differential equations. *International Conference on Artificial Intelligence and Statistics*, 2020.
- [20] Benno Liebchen and Hartmut Löwen. Modeling chemotaxis of microswimmers: From individual to collective behavior. In K. Lindenberg, R. Metzler, and G. Oshanin, editors, *Chemical Kinetics: Beyond the Textbook*, pages 493–516. World Scientific Publishing Europe, London, United Kingdom, 2019.

- [21] Gautam I. Menon. Active matter. In J. Murali Krishnan, Abhijit P. Deshpande, and P. B. Sunil Kumar, editors, *Rheology of Complex Fluids*, pages 193–218. Springer New York, New York, NY, 2010.
- [22] Mykola Novik. torch-optimizer – collection of optimization algorithms for pytorch., January 2020.
- [23] Michael Poli, Stefano Massaroli, Atsushi Yamashita, Hajime Asama, Jinkyoo Park, and Stefano Ermon. Torchdyn: implicit models and neural numerical methods in pytorch. In *Neural Information Processing Systems, Workshop on Physical Reasoning and Inductive Biases for the Real World*, volume 2, 2021.
- [24] Miguel Ruiz-Garcia, C. Miguel Barriuso Gutierrez, Lachlan C. Alexander, Dirk G. A. L. Aarts, Luca Ghiringhelli, and Chantal Valeriani. Discovering dynamic laws from observations: The case of self-propelled, interacting colloids, April 2022.
- [25] Tamás Vicsek, András Czirók, Eshel Ben-Jacob, Inon Cohen, and Ofer Shochet. Novel type of phase transition in a system of self-driven particles. *Physical Review Letters*, 75(6):1226–1229, August 1995.
- [26] Tamás Vicsek and Anna Zafeiris. Collective motion. *Physics Reports*, 517(3-4):71–140, 2012.
- [27] Minjie Wang, Da Zheng, Zihao Ye, Quan Gan, Mufei Li, Xiang Song, Jinjing Zhou, Chao Ma, Lingfan Yu, Yu Gai, Tianjun Xiao, Tong He, George Karypis, Jinyang Li, and Zheng Zhang. Deep graph library: A graph-centric, highly-performant package for graph neural networks. *arXiv:1909.01315*, August 2019.
- [28] Yang You, Jing Li, Sashank Reddi, Jonathan Hseu, Sanjiv Kumar, Srinadh Bhojanapalli, Xiaodan Song, James Demmel, Kurt Keutzer, and Cho-Jui Hsieh. Large batch optimization for deep learning: Training bert in 76 minutes. In *International Conference on Learning Representations*, 2019.

A Supplemental Material

Computational Resources

Detailed specifications of the computational setup are provided here to ensure reproducibility. We employed the Dell Precision 7920 Tower, which comprises of 64 GB RAM, 2 Intel Xeon CPUs, and 2 NVIDIA RTX A6000 GPUs. The system operates under Linux Ubuntu 22.04, with all neural network training processes managed through pyenv with python 3.8.13 to maintain environment consistency. To use the GPUs in the computation, we used CUDA 11.5 and PyTorch 1.13.1.

Existing Assets

To construct our framework, we utilized the Deep Graph Library 1.1.1 (<https://www.dgl.ai/>)[27], TorchSDE 0.2.5 (<https://github.com/google-research/torchsde>)[19, 16], TorchDyn 1.0.4 (<https://github.com/DiffEqML/torchdyn>)[23], and torch-optimizer 0.3.0 (<https://github.com/jettify/pytorch-optimizer>)[22], all of which are publicly available under the MIT License and Apache License 2.0.

Supplemental Tables

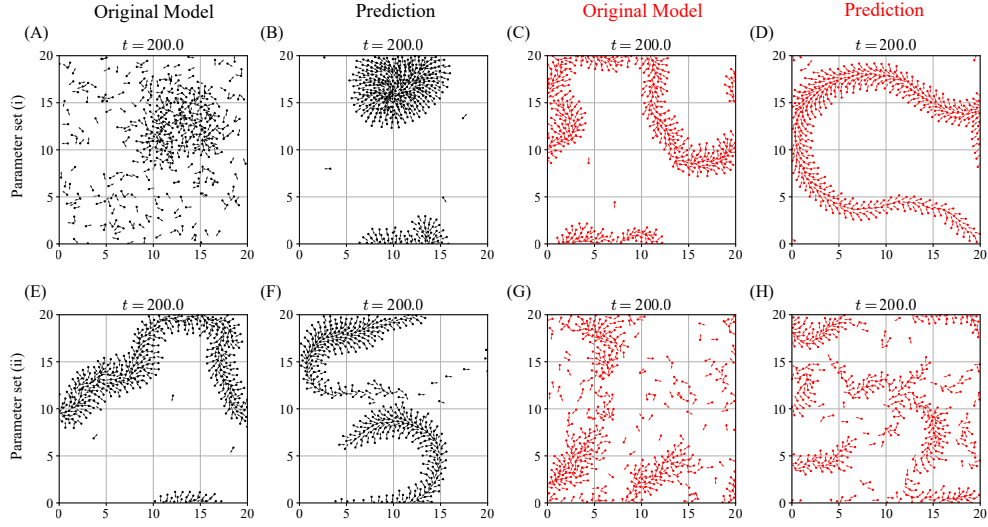
Trial ID	γ	M_{tra}	$\text{MSE}(F_v^{(1)})$	$\text{MAE}(F_v^{(1)})$	$\text{MSE}(F_v^{(2)})$	$\text{MAE}(F_v^{(2)})$
1	1×10^{-2}	270	3.6×10^{-3}	5.9×10^{-2}	5.1×10^{-3}	4.8×10^{-2}
2	1×10^{-2}	3	1.7	1.4	2.2×10^{-2}	1.4×10^{-1}
3	1×10^{-2}	3	9.4	3.7	2.2×10^{-2}	1.3×10^{-1}
4	1×10^{-1}	3	1.2×10^{-2}	1.7×10^{-2}	2.2×10^{-2}	1.0×10^{-1}
5	1×10^{-1}	3	5.4×10^{-2}	3.8×10^{-2}	2.3×10^{-2}	1.1×10^{-1}

Supplemental Table S1: Normalized MSE and MAE of the estimation of $F^{(1)}$ and $F^{(2)}$ for the harmonic interaction model. Each row indicates an independent experiment.

Parameter set	$\alpha_{CF}(0)$	$\alpha_{CF}(1)$	$\alpha_{Ch}(0)$	$\alpha_{Ch}(1)$
(i)	0.1	0.9	2.0	0.2
(ii)	0.9	0.5	0.5	0.5
(iii)	0.9	0.9	0.2	0.2
(iv)	0.9	0.9	0.5	0.5
(v)	0.1	0.1	2.0	2.0

Supplemental Table S2: Parameter sets used in the simulations of the mixed-species model.

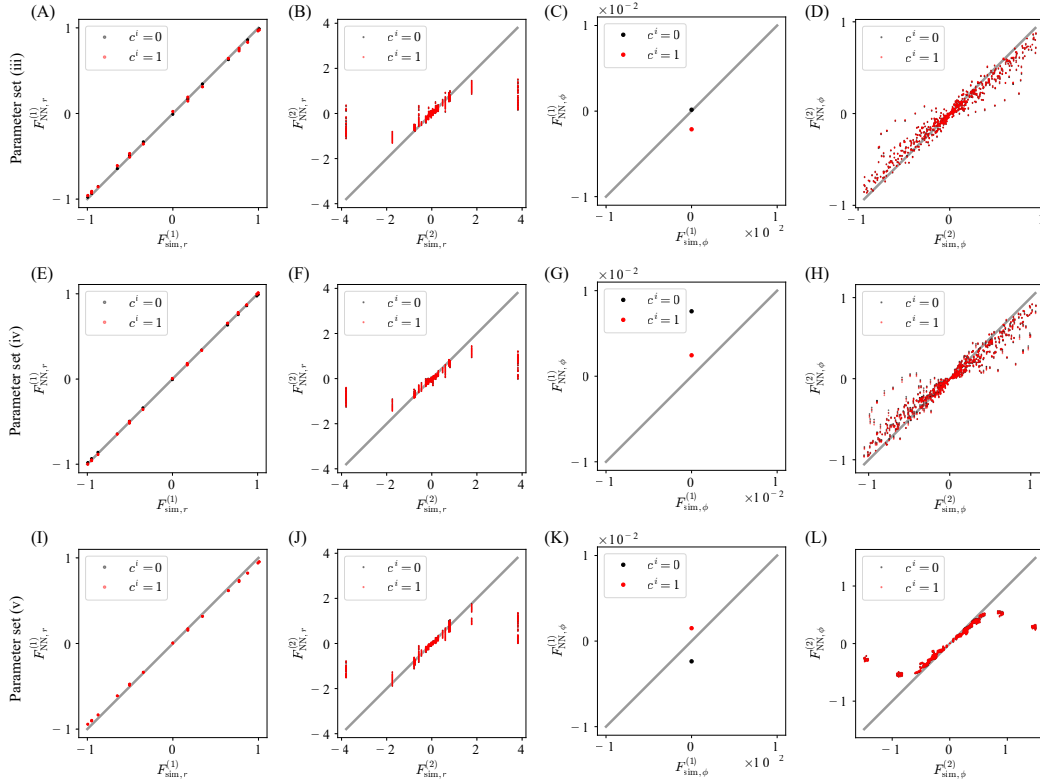
Supplemental figures



Supplemental Figure S1: Snapshots of the simulation results in the mixed-species model and the estimated model. Panels (A, C, E, G) depict results from the mixed-species model, and panels (B, D, F, H) from the estimated model. The upper rows (A-D) represent simulations with parameter set (i), and the lower rows (E-H) with parameter set (ii). Panels (A, B, E, F) include individuals with $c^i = 0$ and panels (C, D, G, H) with $c^i = 1$. Colors correspond to those used in Figure 2.

Trial ID	Parameter set	MSE($F_r^{(1)}$)	MAE($F_r^{(1)}$)	MSE($F_\phi^{(1)}$)	MAE($F_\phi^{(1)}$)	MSE($F_r^{(2)}$)	MAE($F_r^{(2)}$)	MSE($F_\phi^{(2)}$)	MAE($F_\phi^{(2)}$)
1	(i)	1.5×10^{-3}	3.7×10^{-2}	4.5×10^{-7}	6.7×10^{-4}	5.6×10^{-1}	2.7×10^{-1}	2.4×10^{-1}	2.8×10^{-1}
2	(ii)	1.7×10^{-3}	3.5×10^{-2}	3.0×10^{-7}	3.9×10^{-3}	9.9×10^{-1}	3.0×10^{-1}	1.6×10^{-1}	2.8×10^{-1}
3	(ii)	2.0×10^{-3}	4.2×10^{-2}	3.8×10^{-6}	1.7×10^{-3}	1.9×10^{-1}	1.6×10^{-1}	5.4×10^{-2}	2.0×10^{-1}
4	(ii)	5.8×10^{-4}	2.3×10^{-2}	7.1×10^{-6}	2.7×10^{-3}	2.7×10^{-1}	1.7×10^{-1}	5.8×10^{-2}	2.1×10^{-1}
5	(iii)	1.0×10^{-3}	3.1×10^{-2}	2.3×10^{-6}	1.1×10^{-3}	4.2×10^{-1}	1.9×10^{-1}	6.8×10^{-2}	2.5×10^{-1}
6	(iv)	1.6×10^{-4}	1.3×10^{-2}	3.2×10^{-5}	5.0×10^{-3}	3.7×10^{-1}	1.7×10^{-1}	7.3×10^{-2}	2.4×10^{-1}
7	(v)	2.3×10^{-3}	4.8×10^{-2}	3.9×10^{-6}	1.9×10^{-3}	2.8×10^{-1}	1.9×10^{-1}	8.8×10^{-2}	1.6×10^{-1}
8	(v)	6.4×10^{-3}	8.0×10^{-2}	3.1×10^{-5}	5.4×10^{-3}	3.9×10^{-1}	2.3×10^{-1}	1.4×10^{-1}	2.0×10^{-1}

Supplemental Table S3: Normalized MSE and MAE of the estimation of $F^{(1)}$ and $F^{(2)}$ for the mixed-species model. Each row indicates an independent experiment. To note, $\text{MSE}(F_\phi^{(1)})$ and $\text{MAE}(F_\phi^{(1)})$ are not normalized since the true value is zero in any case.



Supplemental Figure S2: The functions estimated from data with the mixed-species model, without dependency on species type, plotted against the true values. The rows display different cases: (A-D) with parameter set (iii), (E-H) with parameter set (iv), and (I-L) with parameter set (v). A gray line serves as a guide to indicate where the estimated values equal the true values.

Supplemental Movies

Supplemental Movie S1:

A visualization of the simulation based on the harmonic interaction model with friction constant $\gamma = 1 \times 10^{-2}$.

Supplemental Movie S2:

A visualization of the simulation based on the harmonic interaction model with friction constant $\gamma = 1 \times 10^{-1}$.

Supplemental Movie S3:

The results of simulations using the estimated functions $F_{\text{NN}}^{(1)}$ and $F_{\text{NN}}^{(2)}$, which were trained using $N_{\text{tra}} = 270$ data from the harmonic interaction model with $\gamma = 1 \times 10^{-2}$.

Supplemental Movie S4:

The results of simulations using the estimated functions $F_{\text{NN}}^{(1)}$ and $F_{\text{NN}}^{(2)}$, which were trained using $N_{\text{tra}} = 3$ data from the harmonic interaction model with $\gamma = 1 \times 10^{-2}$.

Supplemental Movie S5:

The results of simulations using the estimated functions $F_{\text{NN}}^{(1)}$ and $F_{\text{NN}}^{(2)}$, which were trained using $N_{\text{tra}} = 3$ data from the harmonic interaction model with $\gamma = 1 \times 10^{-1}$.

Supplemental Movie S6:

A visualization of the simulation based on the mixed-species model with parameter set (i).

Supplemental Movie S7:

A visualization of the simulation based on the mixed-species model with parameter set (ii).

Supplemental Movie S8:

The results of simulations using the estimated functions $F_{\text{NN}}^{(1)}$ and $F_{\text{NN}}^{(2)}$, which were trained using $N_{\text{tra}} = 3$ data from the mixed-species model with parameter set (i).

Supplemental Movie S9:

The results of simulations using the estimated functions $F_{\text{NN}}^{(1)}$ and $F_{\text{NN}}^{(2)}$, which were trained using $N_{\text{tra}} = 3$ data from the mixed-species model with parameter set (ii).